Large–eddy simulations of a turbulent mixing layer using the stretched–vortex subgrid model

T. W. Mattner

School of Mathematical Sciences
University of Adelaide, South Australia, 5005, AUSTRALIA

Abstract

This paper reports results from a large–eddy simulation of a temporal mixing layer using the stretched–vortex subgrid stress and mixing models. The simulation achieves a Reynolds number of about 2×10^7 when based on the momentum thickness. Linear growth of the momentum thickness and collapse of the mean velocity and scalar concentration profiles suggest that the flow is self–similar. Considerable variability is, however, observed in the Reynolds stress and integrated kinetic–energy dissipation rate.

Introduction

Turbulent mixing is an important fundamental and unresolved problem in fluid mechanics and is crucial in many industrial and scientific contexts. Prediction of many turbulent flows remains impracticable due to the enormous computational resources needed to resolve all relevant scales. This problem is mitigated in a large–eddy simulation where only the large scales are resolved, while the fine subgrid or unresolved scales are modelled.

Pullin and coworkers [7, 12, 8] have developed subgrid stress and mixing models by assuming that the subgrid motion consists of an homogeneous ensemble of stretched spiral vortices. A particularly attractive feature of these models is that it is possible to calculate both resolved and subgrid contributions to statistical quantities. The potential of these models has been demonstrated by recent simulations of compressible Richtmyer–Meshkov instability [3]. Due to the complexity of that flow, the data available for comparison are limited. The purpose of the present work is to apply the subgrid stress and mixing model to a simpler flow for which there is a more comprehensive collection of quantitative high Reynolds–number data available for comparison.

The plane mixing layer is a canonical turbulent flow that forms between two uniform parallel streams of fluid that have different velocities. In experiments, this flow is typically produced by merging two separate streams that are initially separated by a plate. The flow then develops spatially from the trailing edge of the plate. When the streams are opposite in direction and have the same speed, the mixing layer grows in time. Although the spatial and temporal flows are different, useful comparisons are still possible if the velocity ratio of the two streams of the spatial mixing layer is sufficiently close to one [9].

Numerous experimental and numerical studies have established self–similar mixing layers. Unfortunately, in the case of a spatial mixing layer, the ultimate state does not appear to be universal but may depend on inlet boundary conditions [10]. In the case of a temporal mixing layer, this corresponds to a dependence on initial conditions. Conditions for self–similarity include the absence of length scales other than that of the mixing layer thickness, h, as well as sufficiently large Reynolds numbers.

The aim of the present work is to use the stretched–vortex mod-

els to simulate a turbulent temporal mixing layer. To encourage a self–similar flow, the simulation is run at very high Reynolds numbers, well above those typically attained in laboratory investigations or fully–resolved direct numerical simulations. A passive scalar is introduced in order to test the stretched–vortex mixing model. The model produces a flow that is approximately self–similar.

Simulation details

In this simulation, the fluid is assumed to be of uniform density. The equations of motion are obtained by applying a spatial filter to the mass, scalar–transport, and momentum equations. The filtered equations are

$$\frac{\partial \overline{u}_j}{\partial x_j} = 0, \tag{1a}$$

$$\frac{\partial \overline{Y}}{\partial t} + \frac{\partial \overline{u}_j \overline{Y}}{\partial x_j} = \frac{\partial}{\partial x_j}\left(\mathcal{D}\frac{\partial \overline{Y}}{\partial x_j}\right) - \frac{\partial q_j}{\partial x_j}, \tag{1b}$$

$$\frac{\partial \overline{u}_i}{\partial t} + \frac{\partial \overline{u}_i \overline{u}_j}{\partial x_j} = -\frac{\partial \overline{p}/\rho}{\partial x_i} + \frac{\partial \overline{\tau}_{ij}}{\partial x_j} - \frac{\partial T_{ij}}{\partial x_j}, \tag{1c}$$

where x_i and u_i are the components of the Eulerian position and velocity vectors, respectively, Y is the scalar concentration, $\mathcal{D}$ its diffusivity, p is the pressure, τ_{ij} is the viscous stress tensor,

$$\tau_{ij} = \nu\left[\frac{\partial u_i}{\partial x_j} + \frac{\partial u_j}{\partial x_i}\right], \tag{2}$$

and filtered variables are defined by

$$\overline{f} \equiv \int G(x - x') f(x')\, \mathrm{d}x', \tag{3}$$

where G is a filter kernel whose form is implied by the subgrid model. The additional terms,

$$q_j \equiv \overline{u_j Y} - \overline{u}_j \overline{Y}, \tag{4}$$

and

$$T_{ij} \equiv \overline{u_i u_j} - \overline{u}_i \overline{u}_j, \tag{5}$$

are the subgrid–scale scalar flux and subgrid–scale stress, respectively.

Equations (1b) and (1c) are closed using the stretched–vortex subgrid–scale stress model of Misra & Pullin [7] and the stretched–vortex subgrid–scale scalar flux model of Pullin [8]. For a single subgrid vortex, the subgrid–scale stress is

$$T_{ij} = K(\delta_{ij} - e_i e_j) \tag{6}$$

where K is the subgrid kinetic energy per unit mass, and e_i are the components of the unit vector in the direction of the subgrid vortex axis. The subgrid–scale scalar flux is

$$q_j = -\frac{1}{2}\Delta K^{1/2}(\delta_{ij} - e_i e_j)\frac{\partial \overline{Y}}{\partial x_i} \tag{7}$$

where Δ is the local mesh size.

The subgrid kinetic energy is estimated using the spectrum of the Lundgren spiral vortex, that is,

$$K = \int_{k_c}^{\infty} \mathcal{K}_0 \varepsilon^{2/3} k^{-5/3} \exp[-2k^2 \nu/(3|a|)] \, dk, \qquad (8)$$

where k is the wavenumber, $k_c = \pi/\Delta$ is the cutoff wavenumber, $\mathcal{K}_0$ the Kolmogorov prefactor, ε the local cell–averaged dissipation rate, ν the kinematic viscosity, and $|a|$ the axial strain along the subgrid vortex axis [12]. The group $\mathcal{K}_0 \varepsilon^{2/3}$ is estimated from the local resolved second–order velocity structure function using spherical averages [5, 12]. The proportion of subgrid vortices aligned with the principal extensional eigenvector of the resolved rate–of–strain tensor, $\overline{S}_{ij}$, and the resolved vorticity vector, ω, is given by λ and $(1 - \lambda)$, respectively, where

$$\lambda = \lambda_3/(\lambda_3 + ||\omega||) \qquad (9)$$

and λ_3 is the principal extensional eigenvalue (model 1b [7]).

Equation (1) is solved in a cubic domain with side length L. Periodic boundary conditions are applied in the transverse homogeneous directions, x_1 and x_3. The top and the bottom of the box are modelled as impermeable walls moving in opposite directions, that is, $\overline{u}_1/\Delta U = \pm 1/2$ and $\overline{u}_2 = \overline{u}_3 = 0$, where ΔU is the velocity difference between the upper and lower streams. These boundary conditions are only appropriate if the thickness of the mixing zone is much less than the size of the domain. A Fourier spectral collocation scheme is used in the homogeneous directions, x_1 and x_3. An eighth–order compact finite–difference scheme [4] is used in the inhomogeneous direction, x_2. The grid spacing, Δ, is identical in each direction. The grid size is 256^3. Aliasing is minimized by calculating the nonlinear convective terms in skew–symmetric form [2]. A third–order variable–time–step Adams–Bashforth–Moulton scheme is used for temporal integration. The code was validated by computing solutions of the incompressible unsteady Stuart vortex (with the subgrid–scale model turned off and with suitably modified boundary conditions) [11].

The initial mean velocity profile is

$$\frac{u}{\Delta U} = \frac{1}{2} \tanh\left(\frac{y}{\delta}\right), \qquad (10)$$

where δ is set to approximately 3.2Δ. This is perturbed by a random, three–dimensional, divergence–free disturbance whose energy spectrum peaks at $k\ell = 116$, where $\ell = L/2\pi$ and the maximum resolvable wavenumber is $k_c\ell = 128$. The scalar is initialised with the same function as the mean velocity (10), but linearly shifted to obtain $0 \leq \overline{Y} \leq 1$. The scalar field is not perturbed. For this simulation, the Reynolds number, $Re_L \equiv \Delta U L/\nu$, is 10^8 and the Schmidt number, $Sc \equiv \nu/\mathcal{D}$, is 1.

Results and discussion

Visualizations of the scalar field are shown in figure 1 at three selected times. Early in the simulation, large–scale coherent spanwise structures emerge. The wavelength of these structures is much larger than those that dominate the initial perturbation field. Inviscid linear stability theory predicts that, for a hyperbolic–tangent velocity profile, the wavenumber, α, of the most unstable normal modes occur when $\alpha\delta$ is about 0.44 [6]. For the present simulation, this gives about 5.6 structures within the domain, which is quite close to the number observed (about 5). This suggests that initial growth is dominated by inviscid linear instability. The initial growth rate is, however, significantly less than that predicted by linear stability theory, showing
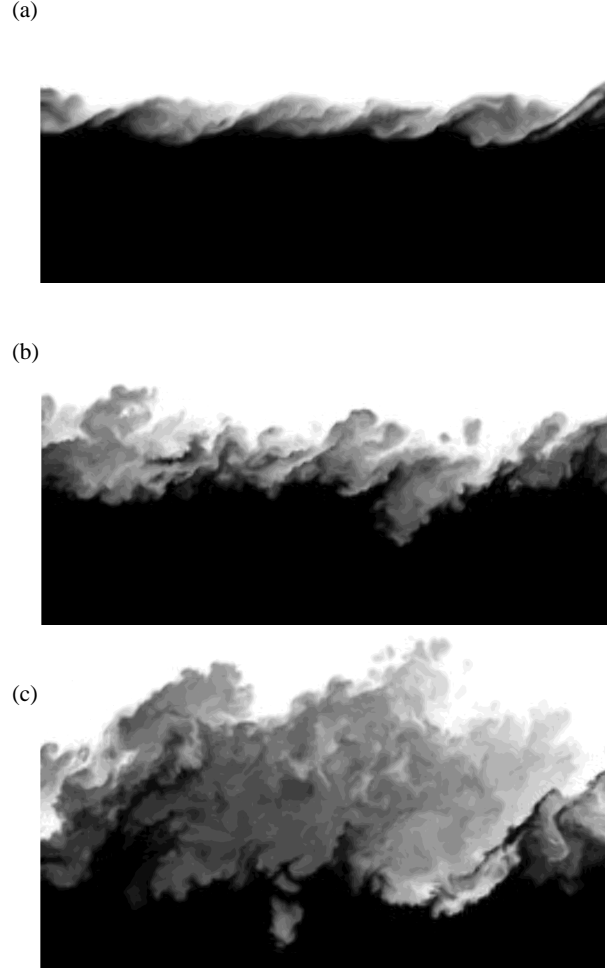
Figure 1: Visualization of the scalar field in the x_1 (horizontal) and x_2 (vertical) plane at the non–dimensional times (a) $\tau = 208$, (b) 320, and (c) 640. Black corresponds to $\overline{Y} = 0$ and white to $\overline{Y} = 1$. Only 60% of the vertical extent of the flow domain is shown.

that the model is already exerting an influence on the flow. The later frames show that this initial regularity does not persist, at least not to the same degree.

In the absence of length scales other than the mixing layer thickness, and at sufficiently high Reynolds numbers, dimensional analysis predicts that the mixing layer thickness grows linearly in time. Mixing–layer thickness is measured in terms of the momentum thickness defined by

$$h_m \equiv \int_{-\infty}^{\infty} \left(\frac{1}{4} - \frac{\langle \overline{u}_1 \rangle}{\Delta U^2}\right) dx_2, \qquad (11)$$

where the angled-brackets denote the plane–average

$$\langle f \rangle (x_2) = \frac{1}{L^2} \iint_{L^2} f(x_1, x_3) \, dx_1 \, dx_3. \qquad (12)$$

The initial thickness is $h_0 = \delta/2$. This is used to define the nondimensional time $\tau \equiv \Delta U t/h_0$. Figure 2 shows that the momentum thickness grows linearly with time after $\tau \approx 200$. Note that the first frame shown in figure 1 corresponds to the beginning of the linear growth phase. Other measures of the mixing–zone thickness, including the vorticity thickness,
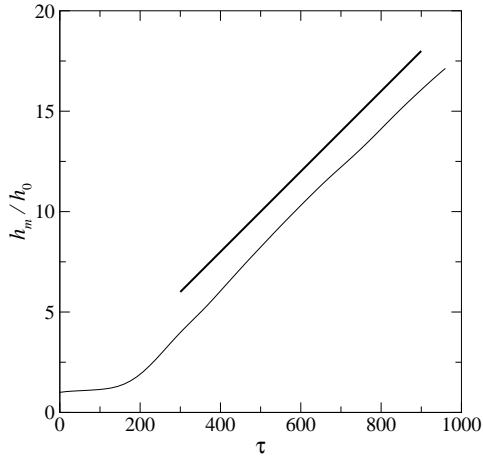
Figure 2: Growth of the normalized momentum thickness versus non–dimensional time. The slope of the bold line is 0.02.

Figure 3: Plane–averaged streamwise component of velocity at $\tau = 208$ (solid), 320 (long–dashed), 480 (dashed), 640 (dot–dashed), 800 (dotted). Symbols are the experimental data of Bell & Mehta [1]. The solid grey line is the initial velocity profile.

$h_\omega \equiv \Delta U/(\partial \overline{u}_1/\partial x_2)_{\max}$, and the scalar mixing–zone width, $h_Y \equiv h_{0.99} - h_{0.01}$, where $\langle \overline{Y} \rangle (h_{0.99}) = 0.99$ and $\langle \overline{Y} \rangle (h_{0.01}) = 0.01$, also grow linearly, albeit with greater variation. The non–dimensional linear growth rate $r \equiv \mathrm{d}(h_m/h_0)/\mathrm{d}\tau$ is approximately 0.02. This is at the high end of the experimental range (0.014 to 0.022) quoted by Rogers & Moser [9].

Further evidence of self–similarity is the collapse of the plane–averaged velocity, $\langle \overline{u}_1 \rangle$, and plane–averaged scalar concentration, $\langle \overline{Y} \rangle$, when plotted against the scaled coordinate, x_2/h_m (figures 3 and 4, respectively). Although the collapse of the velocity profiles is not a sensitive indication of self–similarity [9], it is nevertheless remarkable that the model produces a mean velocity profile that is in accord with the mean velocity profiles measured by Bell & Mehta [1] and the direct numerical simulation data of Rogers & Moser [9]. Although the profiles of scalar concentration exhibit a greater degree of variability than the mean velocity profiles, they are also more clearly distinguished from their initial profile.

More sensitive indicators of self–similarity are profiles of the Reynolds stress tensor in scaled coordinates. These will be presented in entirety elsewhere, however figure 5 shows the contribution of the resolved field to the plane–averaged Reynolds shear stress. In general, the profiles of the Reynolds stress tensor are considerably more variable than the mean velocity profiles, and tend to overpredict the results of Bell & Mehta [1] and Rogers & Moser [9]. The agreement between the simulation results at $\tau = 208$ and the experimental results appears to be coincidental, and is not replicated for the other components of the Reynolds stress tensor.

The integrated subgrid kinetic–energy dissipation rate is

$$\mathcal{E} = \int_{-\infty}^{\infty} \varepsilon \, \mathrm{d}x_2, \tag{13}$$

where $\varepsilon = \langle T_{ij} \overline{S}_{ij} \rangle$ and $\overline{S}_{ij}$ is the resolved–scale rate–of–strain tensor. In the present high Reynolds–number simulation, the subgrid dissipation completely dominates the resolved–scale dissipation and is a good estimate of the total dissipation. In a self–similar flow, the integrated dissipation rate is expected to scale as ΔU^3. Figure 6 shows the evolution of the scaled integrated dissipation rate. This does not approach a constant value in the linear growth phase but oscillates between about 2.5 and 3.5.
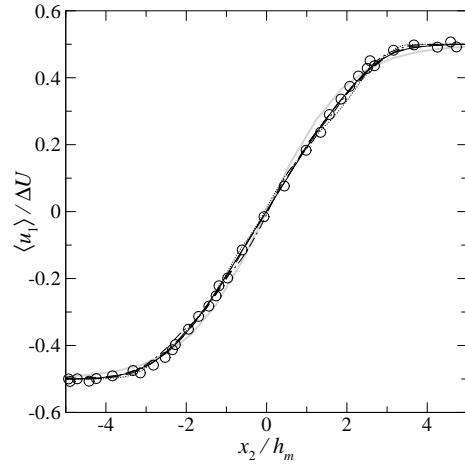
In the present simulation, the local Reynolds number, $Re_m = \Delta U h_m/\nu$, increases from about 10^6 up to 2×10^7. This is considerably higher than Reynolds numbers typically attained in laboratory experiments or direct numerical simulations (for example, the experiments of Bell & Mehta [1] achieve $Re_m \approx 6000$, while the direct numerical simulations of Rogers & Moser [9] achieve $Re_m \approx 2400$). This does not render a comparison with these studies meaningless, for if the flow is truly self–similar, then it should be independent of Reynolds number. Further simulations are being run to investigate model predictions at different Reynolds numbers.

A large–eddy simulation is freed from the resolution requirements dictated by the range of spatial scales generated at high Reynolds number. However, if the aim of the simulation is to produce well–converged statistics of a self–similar flow whose spatial scale grows in time, then there is still a requirement to encompass a range of scales that span the generations of large–scale eddies that develop during the simulation. In the present simulation, only five structures emerged from the initial conditions. This would allow only two 'pairings' or generations of structures to develop before a single structure fills the domain. It is possible that this is insufficient for the flow to become truly independent of its initial conditions and achieve a self–similar state. Furthermore, it is possible that the statistics are not well–converged. This may explain the highly oscillatory value of the integrated dissipation rate. The number of initial structures can be increased by decreasing the thickness of the initial profile, however this is ultimately limited by the need to resolve some portion of the flow. Further decrease of the initial thickness requires a finer grid and therefore larger grid sizes. A more efficient approach to this computational problem may be the use of adaptive mesh refinement.

One issue that is not evident from the statistics concerns the pointwise values of the resolved scalar field. Although an unfiltered scalar field is bounded by its initial maximum and minimum values, a filtered scalar field need not. Indeed, in this simulation it is found that the resolved scalar field, $\overline{Y}$, exceeds its initial bounds in a small proportion of the computational domain. For the passive scalar used in this simulation, this appears to be of little consequence and the scalar excursions are aver-
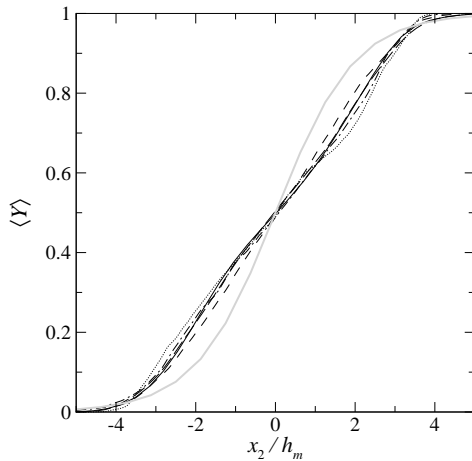
Figure 4: Plane–averaged scalar distribution at $\tau = 208$ (solid), 320 (long–dashed), 480 (dashed), 640 (dot–dashed), 800 (dotted). The solid grey line is the initial scalar profile.
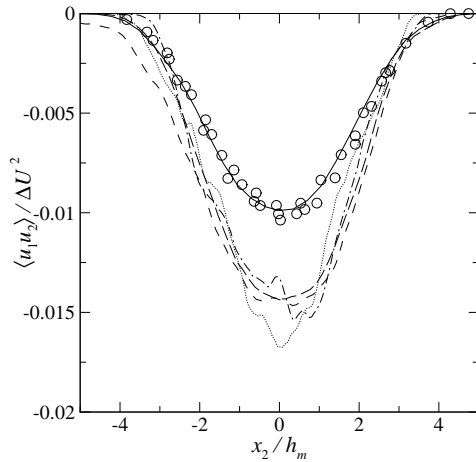
Figure 5: Plane–averaged Reynolds shear stress at $\tau = 208$ (solid), 320 (long–dashed), 480 (dashed), 640 (dot–dashed), 800 (dotted). Symbols are the experimental data of Bell & Mehta [1].
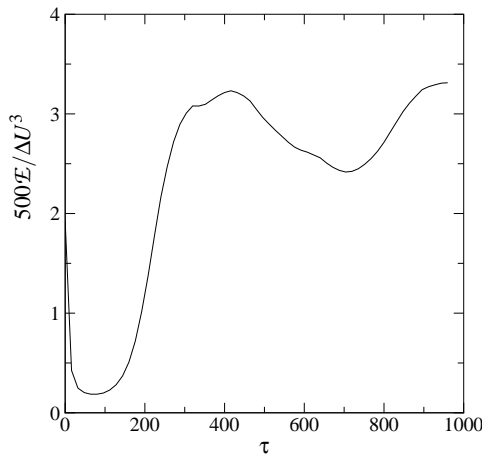
Figure 6: Evolution of the scaled integrated dissipation rate.

aged out in the statistics. However, the current code is written for variable–density incompressible flow, where the density is an active scalar. In that case, it is essential that the scalar not attain zero or negative values, as this quickly leads to failure of the calculation.

Conclusions

A large–eddy simulation of a plane turbulent mixing layer using the stretched–vortex subgrid stress and mixing models achieved a final Reynolds number of $Re_m \approx 2 \times 10^7$. The momentum thickness grows linearly with a non–dimensional growth rate of about 0.02. The mean velocity and mean scalar concentration collapse when plotted against scaled coordinates. These observations are consistent with a flow that is self–similar. However, the components of the Reynolds stress tensor do not collapse as well, and tend to overpredict available data. The integrated dissipation rate does not achieve a stationary value during the simulation.

References

[1] Bell, J. H. and Mehta, R. D., Development of a two-stream mixing layer from tripped and untripped boundary layers, *AIAA Journal*, **28**, 1990, 2034–2042.

[2] Blaisdell, G. A., Spyropoulos, E. T. and Qin, J. H., The effect of the formulation of nonlinear terms on aliasing errors in spectral methods, *Appl. Numer. Math.*, **21**, 1996, 207–219.

[3] Hill, D. J., Pantano, C. and Pullin, D. I., Large-eddy simulation and multiscale modelling of a Richtmyer-Meshkov instability with reshock, *J. Fluid Mech.*, **557**, 2006, 29–61.

[4] Lele, S. K., Compact finite difference schemes with spectral-like resolution, *J. Comp. Phys.*, **103**, 1992, 16–42.

[5] Lesieur, M. and Metais, O., New trends in large-eddy simulations of turbulence, *Annu. Rev. Fluid Mech.*, **28**, 1996, 45–82.

[6] Michalke, A., On the inviscid instability of the hyperbolic-tangent velocity profile, *J. Fluid Mech.*, **19**, 1964, 543–556.

[7] Misra, A. and Pullin, D. I., A vortex-based subgrid stress model for large-eddy simulation, *Phys. Fluids*, **9**, 1997, 2443–2454.

[8] Pullin, D. I., A vortex-based model for the subgrid flux of a passive scalar, *Phys. Fluids*, **12**, 2000, 2311–2319.

[9] Rogers, M. M. and Moser, R. D., Direct simulation of a self-similar turbulent mixing layer, *Phys. Fluids*, **6**, 1994, 903–923.

[10] Slessor, M. D., Bond, C. L. and Dimotakis, P. E., Turbulent shear-layer mixing at high reynolds numbers: effects of inflow conditions, *J. Fluid Mech.*, **376**, 1998, 115–138.

[11] Stuart, J. T., On finite amplitude oscillations in mixing layers, *J. Fluid Mech.*, **29**, 1967, 417–440.

[12] Voekl, T., Pullin, D. I. and Chan, D. C., A physical-space version of the stretched-vortex subgrid-stress model for large-eddy simulation, *Phys. Fluids*, **12**, 2000, 1810–1825.